

A coupled discrete unified gas-kinetic scheme for Boussinesq flows

Peng Wang^a, Shi Tao^a, Zhaoli Guo^{a,*}

^a*State Key Laboratory of Coal Combustion, Huazhong University of Science and Technology, Wuhan, 430074, P.R. China*

Abstract

Recently, the discrete unified gas-kinetic scheme (DUGKS) [Z. L. Guo *et al.*, Phys. Rev. E **88**, 033305 (2013)] based on the Boltzmann equation is developed as a new multiscale kinetic method for isothermal flows. In this paper, a thermal and coupled discrete unified gas-kinetic scheme is derived for the Boussinesq flows, where the velocity and temperature fields are described independently. Kinetic boundary conditions for both velocity and temperature fields are also proposed. The proposed model is validated by simulating several canonical test cases, including the porous plate problem, the Rayleigh-bénard convection, and the natural convection with Rayleigh number up to 10^{10} in a square cavity. The results show that the coupled DUGKS is of second order accuracy in space and can well describe the convection phenomena from laminar to turbulent flows. Particularly, it is found that this new scheme has better numerical stability in simulating high Rayleigh number flows compared with the previous kinetic models.

Keywords: gas-kinetic method, semi-Lagrangian scheme, Boussinesq flows, turbulent natural convection

*Corresponding author.

Email addresses: sklccwangpeng@hust.edu.cn (Peng Wang), lssts1013@hust.edu.cn (Shi Tao), zlguo@hust.edu.cn (Zhaoli Guo)

1. Introduction

In recent years, kinetic methods have drawn particular attention as newly-developing alternative computational fluid dynamics (CFD) technology. Unlike conventional CFD methods based on direct discretizations of the Navier-Stokes equations, kinetic methods are based on the kinetic theory or the micro particle dynamics, which provides the theoretical connection between hydrodynamics and the underlying microscopic physics, and thus provides efficient tools for multiscale flows. Up to date, a variety of kinetic methods have been proposed, such as the lattice gas cellular automata (LGCA) [1], the lattice Boltzmann equation (LBE) [2, 3], the gas-kinetic scheme (GKS) [4, 5, 6, 7], and the smoothed particle hydrodynamics (SPH) [8], among which the GKS and LBE are specifically designed for CFD.

Both GKS and LBE are compressible schemes for hydrodynamic equations based on gas-kinetic models, but the GKS is a finite-volume (FV) scheme originally designed for compressible flows, while LBE is a finite-difference scheme originally designed for nearly incompressible isothermal flows with low Mach number [9, 10]. Later both schemes are extended to low speed thermal flows [11, 12, 13, 14, 15, 16]. Generally, thermal effects in nearly incompressible flows can lead to large compressibility errors for a compressible scheme [12], and in order to reduce such difficulty, the mass and momentum equations are decoupled from the energy equation. Such strategy has been adopted in both GKS and LBE methods [11, 12, 13, 14, 15, 16, 17, 18, 19, 20, 21].

Recently, starting from the Boltzmann equation, a discrete unified gas-kinetic scheme (DUGKS) was proposed for isothermal flows in all Knudsen regimes [6]. The DUGKS is a FV method, which combines the advantages of the GKS in its flux modeling and the LBE methods in its expanded Maxwellian distribution function and discrete conservative collision operator. In addition, the DUGKS has the asymptotic preserving (AP) property in capturing both rarefied and Navier-Stokes equations solutions in the corresponding flow regime [5].

Particularly, although sharing a common kinetic origin, some distinctive features also exist between DUGKS and LBE methods. First, the standard LBE methods can be viewed as special finite-difference schemes, while the DUGKS is a FV one. Second, although both LBE and DUGKS methods evolve in discrete phase space (physical and particle velocity space) and discrete time, in the LBE methods the phase space and time step are coupled due to the particle motion from one node to another one within a time step, whereas the DUGKS does not suffer from this restriction and the time step is fully determined by the Courant-Friedrichs-Lewy (CFL) condition. Third, the streaming process coupling between the discrete velocity and the underlying regular lattice in LBE makes it quite difficult to be extended to non-uniform mesh, while for the DUGKS the non-uniform mesh can be easily employed without additional efforts. More importantly, there are modeling differences in LBE and DUGKS in the particle evolution process. The LBE separates the particle streaming and collision process in its algorithm development. But, the particle transport and collision are fully coupled in DUGKS. This dynamic difference determines the solution deviation in their flow simulations. Consequently, it has been demonstrated that the DUGKS can achieve identical accurate results for the incompressible flows in comparison with the LBE methods, but is more robust and stable [22].

Although the DUGKS has such distinctive features, the original DUGKS is only designed for isothermal flows which limits its applications [6]. The motivation of this work is to develop a DUGKS for near incompressible thermal flows under the decoupling strategy, where the velocity and temperature fields are described by two respective DUGKS models which are coupled under the Boussinesq assumption. Kinetic boundary conditions are also proposed for both the velocity and temperature fields. To validate the performance of the coupled DUGKS, two-dimensional (2D) porous plate problem, the Rayleigh-bénard problem and the natural convection in a square cavity at Rayleigh number from 10^3 up to 10^{10} are simulated.

The rest of this paper is organized as follows. In Sec. 2, the coupled DUGKS

and the kinetic boundary conditions for velocity and temperature fields are developed, some numerical tests are made in Sec. 3 to validate the performance of the new scheme, and a brief summary is presented in Sec. 4.

2. COUPLED DISCRETE UNIFIED GAS-KINETIC SCHEME

In this section, we first introduce the gas-kinetic model for the Boussinesq flows. Then, the DUGKS based on the model will be derived for velocity and temperature fields, respectively. The two evolution equations are coupled based on the Boussinesq assumption. The kinetic boundary conditions and algorithm for velocity and temperature fields are introduced finally.

2.1. Gas-kinetic model for Boussinesq flows

In this subsection, we are going to introduce the gas-kinetic model for the following incompressible Navier-Stokes equations with the thermal effects [12]:

$$\begin{aligned}\frac{\partial \rho}{\partial t} + \nabla \cdot (\rho \mathbf{u}) &= 0, \\ \frac{\partial \mathbf{u}}{\partial t} + \mathbf{u} \cdot \nabla \mathbf{u} &= -\frac{\nabla p}{\rho} + \nu \nabla^2 \mathbf{u} - \mathbf{a}, \\ \frac{\partial T}{\partial t} + \nabla \cdot (T \mathbf{u}) &= \nabla \cdot (\kappa \nabla T),\end{aligned}\tag{1}$$

where ρ , \mathbf{u} , T , p are the density, velocity, temperature and pressure of the flow fluid, respectively, κ is the coefficient of thermal conductivity, and \mathbf{a} is the accelerated velocity of the external force. With the Boussinesq approximation, the force term can be written as:

$$\rho \mathbf{a} = \rho g_0 \beta (T - T_0) \mathbf{y},\tag{2}$$

where g_0 is the gravitational constant, T_0 is the reference temperature, \mathbf{y} is the unit vector in the vertical direction, and β is the coefficient of volume expansion. The gas-kinetic equations corresponding to the above equations can be constructed as [12]:

$$\frac{\partial f}{\partial t} + \boldsymbol{\xi} \cdot \nabla_x f + \mathbf{a} \cdot \nabla_\xi f = \Omega \equiv \frac{f^{eq} - f}{\tau_v},\tag{3}$$

$$\frac{\partial g}{\partial t} + \boldsymbol{\xi} \cdot \nabla g = \Psi \equiv \frac{g^{eq} - g}{\tau_c}, \quad (4)$$

where f and g are the gas distribution functions for the velocity and temperature fields, respectively, and f^{eq} and g^{eq} are the corresponding equilibrium states. Both f and g are functions of space \boldsymbol{x} , time t , and particle velocity $\boldsymbol{\xi}$, and the particle collision time τ_v and τ_c are related to the viscosity and the heat conduction coefficients, respectively. The equilibrium states f^{eq} and g^{eq} take the following forms:

$$f^{eq} = \frac{\rho}{(2\pi RT_1)^{D/2}} \exp\left(-\frac{(\boldsymbol{\xi} - \boldsymbol{u})^2}{2RT_1}\right), \quad (5)$$

$$g^{eq} = \frac{T}{(2\pi RT_2)^{D/2}} \exp\left(-\frac{(\boldsymbol{\xi} - \boldsymbol{u})^2}{2RT_2}\right), \quad (6)$$

where R is the gas constant, T_1 and T_2 are the constant variances which determine the artificial sound speed of the velocity. For continuum flows, the external force term can be approximated as [11]:

$$\boldsymbol{a} \cdot \nabla_{\boldsymbol{\xi}} f \approx \boldsymbol{a} \cdot \nabla_{\boldsymbol{\xi}} f^{eq} = -\frac{\boldsymbol{a} \cdot (\boldsymbol{\xi} - \boldsymbol{u})}{RT_1} f^{eq}. \quad (7)$$

Using the Chapman-Enskog expansion, the hydrodynamic equations (Eq. (1)) can be obtained from Eq. (3) and Eq. (4) exactly in the incompressible limit, with the viscosity coefficient

$$\nu = \tau_v RT_1, \quad (8)$$

and the heat conduction coefficient

$$\kappa = \tau_c RT_2. \quad (9)$$

Therefore, the Prandtl number Pr can be modified by choosing appropriate τ_v , τ_c , T_1 , and T_2 , which gives:

$$\text{Pr} = \frac{\nu}{\kappa} = \frac{\tau_v T_1}{\tau_c T_2}. \quad (10)$$

2.2. DUGKS for velocity

Unlike most of other kinetic methods, the DUGKS is a semi-Lagrangian FV scheme, where the evolution process is under the Eulerian framework and the

flux construction at the cell interface is based on the Lagrangian perspective. It is noted that the original DUGKS does not consider external force term. Hence, in order to model the velocity with a body force, we rewrite Eq. (3) as:

$$\frac{\partial f}{\partial t} + \boldsymbol{\xi} \cdot \nabla_x f = \bar{\Omega} \equiv \Omega + F, \quad (11)$$

where

$$F = a \cdot \nabla_{\boldsymbol{\xi}} f \approx \frac{\mathbf{a} \cdot (\boldsymbol{\xi} - \mathbf{u})}{RT_1} f^{eq}. \quad (12)$$

Notice that $\int F d\boldsymbol{\xi} = 0$, and $\int F \boldsymbol{\xi} d\boldsymbol{\xi} = \rho \mathbf{a}$.

As a FV scheme, in the DUGKS the computational domain is divided into a set of control volumes. Integrating Eq. (11) over a control volume V_j centered at \mathbf{x}_j from time t_n to t_{n+1} (the time step $\Delta t = t_{n+1} - t_n$ is assumed to be a constant in the present work), and using the midpoint rule for the integration of the flux term at the cell interface and trapezoidal rule for the collision term inside each cell, the evolution equation for velocity can be written as [6]:

$$\tilde{f}_j^{n+1} = \tilde{f}_j^{+,n} - \frac{\Delta t}{|V_j|} F^{n+1/2}, \quad (13)$$

where

$$F^{n+1/2} = \int_{\partial V_j} (\boldsymbol{\xi} \cdot \mathbf{n}) f(\mathbf{x}, t_{n+1/2}) d\mathbf{S} \quad (14)$$

is the microflux across the cell interface, \mathbf{n} is the unit vector normal to the cell interface and

$$\tilde{f} = f - \frac{\Delta t}{2} \bar{\Omega}, \quad \tilde{f}^+ = f + \frac{\Delta t}{2} \bar{\Omega} \quad (15)$$

are the auxiliary distributions related to the original distribution function f and the equilibrium distribution function f^{eq} . Clearly, the evolution process is Eulerian. Based on the compatibility condition and the relation of f and \tilde{f} , the density and velocity can be computed by:

$$\rho = \int \tilde{f} d\boldsymbol{\xi}, \quad \rho \mathbf{u} = \int \boldsymbol{\xi} \tilde{f} d\boldsymbol{\xi} + \frac{\Delta t}{2} \rho \mathbf{a}. \quad (16)$$

The key procedure in updating \tilde{f} is to evaluate the microflux $F^{n+1/2}$, which can be solely determined by the gas distribution function $f(\mathbf{x}, t_{n+1/2})$ at the cell interface. The Lagrangian perspective is applied in the construction of

$f(\mathbf{x}, t_{n+1/2})$. To this end, Eq. (11) is integrated within a half time step $h = \Delta t/2$ along the characteristic line with the end point (\mathbf{x}_b) located at the cell interface, and the trapezoidal rule is applied to evaluate the collision term,

$$f(\mathbf{x}_b, \boldsymbol{\xi}, t_n + h) - f(\mathbf{x}_b - \boldsymbol{\xi}h, \boldsymbol{\xi}, t_n) = \frac{h}{2} [\bar{\Omega}(\mathbf{x}_b, \boldsymbol{\xi}, t_n + h) + \bar{\Omega}(\mathbf{x}_b - \boldsymbol{\xi}h, \boldsymbol{\xi}, t_n)]. \quad (17)$$

In order to remove the implicity of Eq. (17), two auxiliary distribution functions are introduced,

$$\bar{f} = f - \frac{h}{2}\bar{\Omega}, \quad \bar{f}^+ = f + \frac{h}{2}\bar{\Omega}. \quad (18)$$

Note that the particle collision effect is included in the above evaluation of the interface gas distribution function. This is the key for the success of the DUGKS [22]. With the newly introduced distribution functions, Eq. (17) can be rewritten as:

$$\bar{f}(\mathbf{x}_b, \boldsymbol{\xi}, t_n + h) = \bar{f}^+(\mathbf{x}_b - \boldsymbol{\xi}h, \boldsymbol{\xi}, t_n). \quad (19)$$

For smooth flows, $\bar{f}^+(\mathbf{x}_b - \boldsymbol{\xi}h, \boldsymbol{\xi}, t_n)$ can be approximated by its Taylor expansion around the cell interface \mathbf{x}_b ,

$$\bar{f}^+(\mathbf{x}_b - \boldsymbol{\xi}h, \boldsymbol{\xi}, t_n) = \bar{f}^+(\mathbf{x}_b, \boldsymbol{\xi}, t_n) - h\boldsymbol{\xi} \cdot \boldsymbol{\sigma}_b, \quad (20)$$

where $\boldsymbol{\sigma}_b = \nabla \bar{f}^+(\mathbf{x}_b, \boldsymbol{\xi}, t_n)$. Based on Eqs. (19) and (20), one can get:

$$\bar{f}(\mathbf{x}_b, \boldsymbol{\xi}, t_n + h) = \bar{f}^+(\mathbf{x}_b, \boldsymbol{\xi}, t_n) - h\boldsymbol{\xi} \cdot \boldsymbol{\sigma}_b. \quad (21)$$

Then, based on the compatibility condition and the relation of f and \bar{f} , the density and velocity at the cell interface can be obtained:

$$\rho = \int \bar{f} d\boldsymbol{\xi}, \quad \rho \mathbf{u} = \int \boldsymbol{\xi} \bar{f} d\boldsymbol{\xi} + \frac{h}{2} \rho \mathbf{a}, \quad (22)$$

from which the equilibrium distribution function $f^{eq}(\mathbf{x}_b, \boldsymbol{\xi}, t_n + h)$ at the cell interface can be obtained. Therefore, based on Eq. (18) and the obtained equilibrium state, the original distribution function at the cell interface can be extracted from \bar{f} ,

$$f(\mathbf{x}_b, t_n + h) = \frac{2\tau_v}{2\tau_v + h} \bar{f}(\mathbf{x}_b, t_n + h) + \frac{h}{2\tau_v + h} f^{eq}(\mathbf{x}_b, t_n + h) + \frac{\tau_v h}{2\tau_v + h} F, \quad (23)$$

from which the interface flux can be evaluated.

As a result, the update of the distribution function \tilde{f} can be done according to Eq. (13). In practical computations, we only need to track the evolution of \tilde{f} , and the required variables in the evolution are:

$$\bar{f}^+ = \frac{2\tau_v - h}{2\tau_v + \Delta t} \tilde{f} + \frac{3h}{2\tau_v + \Delta t} f^{eq} + \frac{3h\tau_v}{2\tau_v + \Delta t} F, \quad (24)$$

$$\tilde{f}^+ = \frac{4}{3} \bar{f}^+ - \frac{1}{3} \tilde{f}. \quad (25)$$

Up to this point, the scheme is designed with the continuous velocity space $\boldsymbol{\xi}$, while the discrete particle velocities $\boldsymbol{\xi}_i$ is employed in DUGKS. Similar to LBE, for low Mach number flows, the Maxwellian distribution can be approximated by its Taylor expansion around zero particle velocity,

$$f_i^{eq} = W_i \rho \left[1 + \frac{\boldsymbol{\xi} \cdot \mathbf{u}}{RT_1} + \frac{(\boldsymbol{\xi} \cdot \mathbf{u})^2}{2(RT_1)^2} - \frac{|\mathbf{u}|^2}{2RT_1} \right], \quad (26)$$

where $f_i^{eq} = w_i f^{eq}(\boldsymbol{\xi}_i)$, $w_i = W_i (2\pi RT_1)^{D/2} \exp\left(-\frac{|\boldsymbol{\xi}_i|^2}{2RT_1}\right)$, and W_i is the weight coefficients corresponding to the abscissas $\boldsymbol{\xi}_i$.

2.3. DUGKS for temperature field

A DUGKS model for Eq. (4) can be constructed similarly. The Eq. (4) is first integrated at the same control volume V_j from t_n to t_{n+1} , and then the same integration rules are employed to approximate the convection term and collision term as that in the velocity, one can get:

$$g_j^{n+1} - g_j^n + \frac{\Delta t}{|V_j|} F^{n+1/2} = \frac{\Delta t}{2} [\Psi_j^{n+1} + \Psi_j^n], \quad (27)$$

where F is the microflux,

$$F^{n+1/2} = \int_{\partial V_j} (\boldsymbol{\xi} \cdot \mathbf{n}) g(\mathbf{x}, t_{n+1/2}) d\mathbf{S}, \quad (28)$$

g_j^n and Ψ_j^n are the cell-averaged values of the distribution function and the collision term, respectively, e.g.,

$$g_j^n = \frac{1}{|V_j|} \int_{V_j} g(\mathbf{x}, t_n) d\mathbf{x}. \quad (29)$$

Two auxiliary distribution functions are introduced to remove the implicity in Eq. (27), then the evolution equation of Eq. (4) can be written as:

$$\tilde{g}_j^{n+1} = \tilde{g}_j^{+,n} - \frac{\Delta t}{|V_j|} F^{n+1/2}, \quad (30)$$

where

$$\tilde{g} = g - \frac{\Delta t}{2} \Psi, \quad \tilde{g}^+ = g + \frac{\Delta t}{2} \Psi, \quad (31)$$

from which the temperature can be computed as:

$$T = \int \tilde{g} d\xi. \quad (32)$$

In order to evaluate the microflux F , we also integrate Eq. (4) within a half time step h along the characteristic line with the end point \mathbf{x}_b at the cell interface, and use the trapezoidal rule to evaluate the collision term,

$$g(\mathbf{x}_b, \boldsymbol{\xi}, t_n + h) - g(\mathbf{x}_b - \boldsymbol{\xi}h, \boldsymbol{\xi}, t_n) = \frac{h}{2} [\Psi(\mathbf{x}_b, t_n + h) + \Psi(\mathbf{x}_b - \boldsymbol{\xi}h, t_n)]. \quad (33)$$

Also another two new distribution functions are introduced to remove the implicity in the above equation,

$$\bar{g} = g - \frac{h}{2} \Psi, \quad \bar{g}^+ = g - \frac{h}{2} \Psi. \quad (34)$$

Then, Eq. (33) can be rewritten as:

$$\begin{aligned} \bar{g}(\mathbf{x}_b, \boldsymbol{\xi}, t_n + h) &= \bar{g}^+(\mathbf{x}_b - \boldsymbol{\xi}h, \boldsymbol{\xi}, t_n) \\ &= \bar{g}^+(\mathbf{x}_b, \boldsymbol{\xi}, t_n) - h\boldsymbol{\xi} \cdot \bar{\boldsymbol{\sigma}}_b, \end{aligned} \quad (35)$$

where $\bar{\boldsymbol{\sigma}}_b = \nabla \bar{g}^+(\mathbf{x}_b, \boldsymbol{\xi}, t_n)$ and the Taylor expansion is made around the cell interface \mathbf{x}_b . Based on Eq. (34) and the compatibility condition, the temperature at the cell interface can be computed as:

$$T = \int \bar{g} d\xi. \quad (36)$$

Together with the conserved variables in velocity, the equilibrium distribution function $g^{eq}(\mathbf{x}_b, \boldsymbol{\xi}, t_n + h)$ can be fully determined. Then, the original distribution function can be obtained,

$$g(\mathbf{x}_b, t_n + h) = \frac{2\tau_c}{2\tau_c + h} \bar{g}(\mathbf{x}_b, t_n + h) + \frac{h}{2\tau_c + h} g^{eq}(\mathbf{x}_b, t_n + h), \quad (37)$$

from which the interface numerical flux \overline{F} can be evaluated.

In computation, it only needs to follow the evolution of \tilde{g} in Eq. (30). The required variables for its evolution are determined by

$$\bar{g}^+ = \frac{2\tau_c - h}{2\tau_c + \Delta t} \tilde{g} + \frac{3h}{2\tau_c + \Delta t} g^{eq}, \quad (38)$$

$$\tilde{g}^+ = \frac{4}{3} \bar{g}^+ - \frac{1}{3} \tilde{g}. \quad (39)$$

In the present work, the DUGKS for temperature field uses the same discrete velocity set as that for velocity field, and the expanded discrete equilibrium distribution function can be written as:

$$g_i^{eq} = W_i T \left[1 + \frac{\boldsymbol{\xi} \cdot \mathbf{u}}{RT_2} + \frac{(\boldsymbol{\xi} \cdot \mathbf{u})^2}{2(RT_2)^2} - \frac{|\mathbf{u}|^2}{2RT_2} \right], \quad (40)$$

where $g_i^{eq} = w_i g^{eq}(\boldsymbol{\xi}_i)$, $w_i = W_i (2\pi RT_2)^{D/2} \exp\left(-\frac{|\boldsymbol{\xi}_i|^2}{2RT_2}\right)$, and W_i is the weight coefficient corresponding to the abscissas $\boldsymbol{\xi}_i$.

2.4. Kinetic boundary conditions

Boundary condition plays an important role in kinetic models in that they will influence their accuracy and stability [23, 24]. In the previous study, two types of kinetic boundary conditions for velocity without external force have been specified in DUGKS [6], among which the bounce-back rule that assumes a particle just reverses its velocity after hitting the wall is presented for no-slip boundary,

$$f(\mathbf{x}_w, \boldsymbol{\xi}_i, t+h) = f(\mathbf{x}_w, -\boldsymbol{\xi}_i, t+h) + 2\rho_w \frac{W_i}{w_i} \frac{\boldsymbol{\xi}_i \cdot \mathbf{u}_w}{RT_1}, \quad \boldsymbol{\xi}_i \cdot \mathbf{n} > 0, \quad (41)$$

where ρ_w and \mathbf{u}_w are the density and velocity at the wall, respectively, and \mathbf{n} is the unit vector normal to the wall pointing to the cell. However, in practical calculations, the walls are fixed at the cell interface, thereby \bar{f} and \bar{g} are needed when dealing with the boundary conditions. For the velocity field, we should give $\bar{f}(\mathbf{x}_w, \boldsymbol{\xi}_i, t)$ other than $f(\mathbf{x}_w, \boldsymbol{\xi}_i, t)$ in the boundary condition, and Eq. (41) can be rewritten as:

$$\bar{f}(\mathbf{x}_w, \boldsymbol{\xi}_i, t+h) = \bar{f}(\mathbf{x}_w, -\boldsymbol{\xi}_i, t+h) + 2\rho_w \frac{W_i}{w_i} \frac{\boldsymbol{\xi}_i \cdot \mathbf{u}'_w}{RT_1}, \quad \boldsymbol{\xi}_i \cdot \mathbf{n} > 0, \quad (42)$$

where $\mathbf{u}'_w = \mathbf{u}_w - (h/2)\mathbf{a}$. For nearly incompressible flow, ρ_w can be approximated well by the constant average density.

As for temperature field, we consider two types of boundaries i.e., wall with a fixed temperature and adiabatic wall. First, for the constant temperature boundary, the distribution function $\bar{g}(\mathbf{x}_w, \boldsymbol{\xi}_i, t)$ for particle leaving the wall can be constructed as [25]:

$$\bar{g}(\mathbf{x}_w, \boldsymbol{\xi}_i, t+h) = -\bar{g}(\mathbf{x}_w, -\boldsymbol{\xi}_i, t+h) + 2\frac{W_i}{w_i}T_w \left[1.0 + \frac{(\boldsymbol{\xi}_i \cdot \mathbf{u}_w)^2}{2(RT_2)^2} - \frac{|\mathbf{u}_w|^2}{2RT_2} \right], \boldsymbol{\xi}_i \cdot \mathbf{n} > 0, \quad (43)$$

where T_w is the wall temperature. Second, the adiabatic boundary, which is a Neumann boundary condition, can be realized by the bounce-back rule [17],

$$\bar{g}(\mathbf{x}_w, \boldsymbol{\xi}_i, t+h) = \bar{g}(\mathbf{x}_w, -\boldsymbol{\xi}_i, t+h). \quad (44)$$

The distribution function $\bar{g}(\mathbf{x}_w, \boldsymbol{\xi}_i, t+h)$ for particle moving towards the wall, i.e., $\boldsymbol{\xi}_i \cdot \mathbf{n} \leq 0$, can be constructed following the procedure described in Sec. 2.3.

2.5. Algorithm

In this subsection, we list the computational procedures for the updating of the discrete distribution functions in both the velocity and temperature fields. In the computation, the weight coefficients w_i are absorbed into the discrete functions, i.e.,

$$f_i = w_i f(\boldsymbol{\xi}_i), \quad g_i = w_i g(\boldsymbol{\xi}_i). \quad (45)$$

Note that the distributions \tilde{f} and \tilde{g} are recorded instead of the original one, respectively, so that the macroscopic variables can be evaluated as:

$$\rho = \sum_i \tilde{f}_i, \quad \rho \mathbf{u} = \sum_i \boldsymbol{\xi}_i \tilde{f}_i + \frac{\Delta t}{2} \rho \mathbf{a}, \quad T = \sum_i \tilde{g}_i. \quad (46)$$

The updates of \tilde{f} and \tilde{g} are same as that for the continuous cases presented in Secs. 2.2 and 2.3. Specially with initialized $\tilde{f}_{j,i}^0$ and $\tilde{g}_{j,i}^0$ in all cells centered at \mathbf{x}_j , the procedure of the DUGKS at each time t_n reads as follows:

(1) Compute the distribution functions $\tilde{f}_{j,i}^{+,n}$ (Eq. (24)) and $\tilde{g}_{j,i}^{+,n}$ (Eq. (38)) in each cell.

- (2) Compute the distribution functions $\bar{f}_i^{n+1/2}(\mathbf{x}_b)$ (Eqs. (21)) and $\bar{g}_i^{n+1/2}(\mathbf{x}_b)$ (Eq. (35)).
- (3) Compute the original distribution functions $f_i^{n+1/2}(\mathbf{x}_b)$ (Eq. (23)) and $f_i^{n+1/2}(\mathbf{x}_b)$ (Eq. (37)).
- (4) Compute the microflux across the cell interfaces from $f_i^{n+1/2}(\mathbf{x}_b)$ (Eq. (14)) and $f_i^{n+1/2}(\mathbf{x}_b)$ (Eq. (28)).
- (4) Update the distribution functions $\bar{f}_{j,i}^{+,n}$ and $\bar{g}_{j,i}^{+,n}$ via Eqs. (13) and (30), respectively, where \tilde{f}^+ and \tilde{g}^+ are computed respectively according to Eqs. (25) and (39).

3. NUMERICAL RESULTS

In this section, several numerical simulations are conducted to validate the proposed model, including the porous plate problem, the Rayleigh-bénard convection, and the natural convection in a square cavity. In our simulations, $T_1 = T_2 = T_0$ are taken for f^{eq} and g^{eq} although they can be different in theory, and the three-point Gauss-Hermite quadrature is used to evaluate the moments, which yields the following discrete velocities and associated weights,

$$\begin{aligned} \xi_{-1} &= -\sqrt{3RT_0}, \quad \xi_0 = 0, \quad \xi_1 = \sqrt{3RT_0}, \\ W_0 &= 2/3, \quad W_{\pm 1} = 1/6. \end{aligned} \tag{47}$$

For the two-dimensional problems considered in this paper, the discrete velocities and weights used in the DUGKS are generated using the tensor product method [6].

In the following simulations, the Mach number is defined as $Ma = U/c_s$, where $U = \sqrt{g_0\beta\Delta TH}$ is the characteristic velocity of the flow, $c_s = \sqrt{RT_0}$ is the speed of sound, ΔT is the temperature difference, and H is the characteristic length; the collision time are determined by $\tau_v = \mu/p$ and $\tau_c = \tau_v/Pr$, where μ is the dynamic viscosity, $p = \rho RT_0$ is the pressure; the time step Δt is determined by the CFL number, i.e., $\Delta t = \eta\Delta x_{min}/C$, where η is the CFL number, Δx_{min} is minimum grid spacing, and C is on the order of the maximal discrete velocity; uniform meshes are adopted for most of the test cases except

for the turbulent natural convection flow where a non-uniform mesh is applied with the requirement of the local accuracy; we set $g_0\beta = 0.1$ and $\eta = 0.5$ in what follows unless otherwise stated; for the steady state cases, the working criterion is defined by:

$$\frac{\sqrt{\sum \|\mathbf{u}(t) - \mathbf{u}(t - 1000\Delta t)\|^2}}{\sqrt{\sum \|\mathbf{u}(t)\|^2}} < 10^{-12} \quad (48)$$

$$\max |T(t) - T(t - 1000\Delta t)| < 10^{-6}.$$

Note that all the parameters employed in our simulations are non-dimensional.

3.1. Porous plate problem

We first study the accuracy of the coupled DUGKS model by simulating the porous plate problem, which has an analytic solution. The problem considered is a channel flow where the upper cool plate with a constant temperature T_c moves with a constant velocity u_0 , and a constant normal flow is injected with a constant velocity v_0 through the bottom hot plate with a constant temperature T_h and withdraw with the same rate from the upper plate. This problem models a fluid being sheared between two plates through which an identical fluid is being injected normal to the shearing direction. The analytic solutions of horizontal velocity and temperature for this problem in steady state are given by [13]:

$$u = u_0 \left(\frac{e^{\text{Re } y/H} - 1}{e^{\text{Re}} - 1} \right), \quad (49)$$

$$T = T_h - \Delta T \left(\frac{e^{\text{Pr Re } y/H} - 1}{e^{\text{Pr Re}} - 1} \right), \quad (50)$$

where Re is the Reynolds number based on the inject velocity v_0 , $\Delta T = T_h - T_c$ is the temperature difference between the hot and cool walls, and $\text{Ra} = g_0\beta\Delta TH^3/(\nu\kappa)$ is the Rayleigh number.

In our simulations, we set $\Delta T = 1.0$ and $u_0 = 0.1$; the length and the height of the channel are $L = 2$ and $H = 1$, respectively. Boundary conditions presented in Sec. 2.4 are applied to the plates, and periodic boundary conditions are applied to inlet and outlet of the channel. In order to evaluate the accuracy of the coupled DUGKS, a set of simulations with different mesh resolutions are

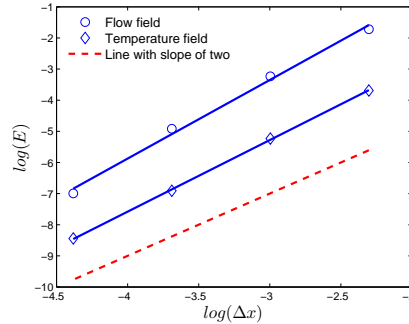


Figure 1: Numerical error versus grid size for the porous plate flow. The slope of the dashed line is 2.

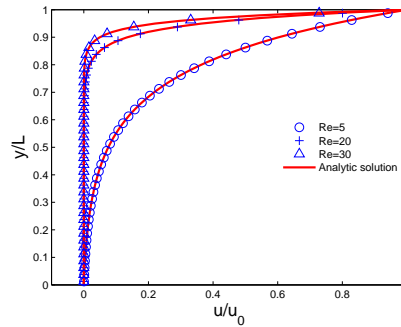


Figure 2: Velocity profiles at $Re = 5, 20$ and 30 of the porous plate problem with $Pr = 0.71, Ra = 100$.

conducted. We use $Pr = 0.71, Re = 10, Ra = 100$, and the grid size varies from $1/10$ to $1/80$, $RT_0 = 100$ so that the time step Δt is small enough to reduce the time error in the evaluation of spatial accuracy and the flow can be treated as incompressible. Moreover, the CFL number is adjusted to keep the time step constant. The relative global error in velocity and temperature fields is defined as:

$$E = \frac{\sqrt{\sum \|A(\mathbf{x}) - A^*(\mathbf{x})\|^2}}{\sqrt{\sum \|A^*(\mathbf{x})\|^2}}, \quad (51)$$

where A (u or T) is the numerical result, A^* is the analytic solution given by Eqs. (49) and (50). The errors in velocity and temperature fields are shown in Fig. 1, which shows that the coupled DUGKS is of second-order accuracy in

space.

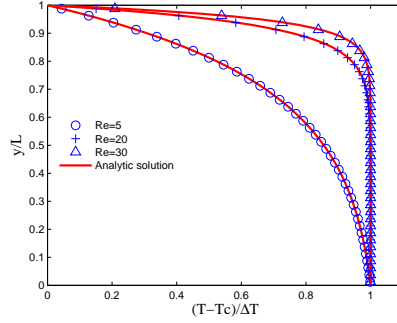


Figure 3: Temperature profiles at $Re = 5, 20$ and 30 of the porous plate problem with $Pr = 0.71, Ra = 100$.

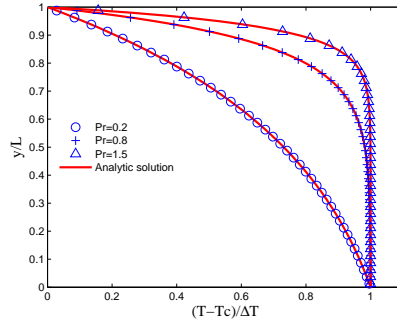


Figure 4: Temperature profiles at $Pr = 0.2, 0.8$ and 1.5 of the porous plate problem with $Re = 10, Ra = 100$.

In addition, a set of simulations with variable Re and Pr are also carried out to validate the new model. Uniform mesh with resolution of $N_x \times N_y = 80 \times 40$ is employed, and RT_0 is set to be 1.0 so that the flow can be regarded as incompressible. Figs. 2 and 3 show the normalized velocity and the temperature profiles respectively for $Pr = 0.71$ and $Ra = 100$ with three sets of Reynolds numbers ($Re = 5, 20$ and 30). Figures. 4 shows the temperature profiles for $Ra = 100$ and $Re = 10$ with three sets of Prandtl numbers ($Pr = 0.2, 0.8$ and 1.5). The analytic solutions are also included for comparison. As shown, the numerical results are in excellent agreement with the analytic ones.

3.2. Rayleigh-Bénard Convection

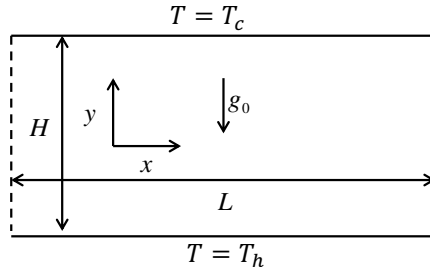


Figure 5: Schematic of the Rayleigh-bénard convection.

The Rayleigh-Bénard convection is a typical Boussinesq flow. As sketched in Fig. 5, the flow domain is a rectangle with length L and height H ($L = 2H$) and a hot wall on the bottom and a cool wall on the top. The Rayleigh number of this flow is defined by $\text{Ra} = g_0 \beta \Delta T H^3 / (\nu \kappa)$ where ΔT is the temperature difference between the hot and the cool walls.

In the simulations, ΔT is set to be 1.0, and RT_0 is set to be 10 so that the code works in the nearly incompressible regime; boundary conditions developed in Sec. 2.4 are applied to the top and bottom walls, and periodic boundary conditions are applied to the two side boundaries; the Prandtl number is fixed at 0.71 (air) in all cases.

Table 1: Critical Rayleigh numbers with different mesh resolutions.

Mesh	Ra_c	Error
40×20	1728.68	1.22%
80×40	1711.50	0.22%
160×80	1706.00	0.11%
Theory[26]	1707.76	

We first measure the critical Rayleigh number Ra_c , at which the static conductive state becomes unstable. Computations are started from the static conductive state at two Rayleigh numbers 1720 and 1735 close to Ra_c . An initial small perturbation is applied to the initial temperature field. The growth rates of the disturbance are measured and extrapolated to obtain the critical Rayleigh

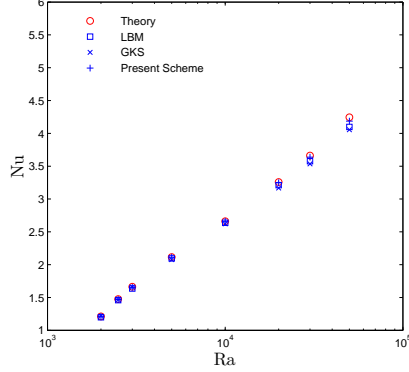


Figure 6: The dependence of average Nusselt number on Rayleigh number. The simulation results by the theoretical analysis [27], the original GKS [12], and the LBE method [16] are also included .

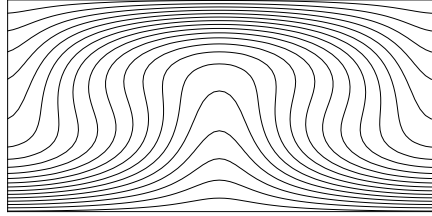
number corresponding to zero growth rate. Table 1 compiles the calculated critical Rayleigh number on different mesh resolutions and its relative errors compared with the result obtained by linear stability theory [26]. It is clearly observed that the coupled DUGKS gives an accurate prediction for the critical Rayleigh number.

Once the Rayleigh-Bénard convection is stabilized, the heat transfer between the top and bottom is greatly enhanced, which can be quantified by the volume average Nusselt number,

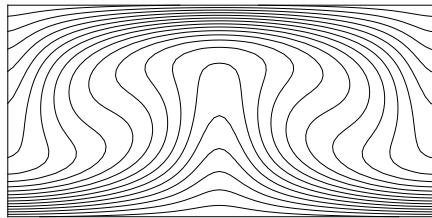
$$\overline{\text{Nu}} = 1 + \frac{\langle vT \rangle}{\kappa \Delta T / H}, \quad (52)$$

where v is the vertical velocity and $\langle \cdot \rangle$ represents the average over the whole flow domain. Figure. 6 illustrates the calculated relationship between the average Nusselt number and the Rayleigh number with mesh resolution of 80×40 . Also included are the results given by theoretical analysis [27], the original GKS [12], and the LBE [16]. As is shown, our results agree well with theoretical results [27] and is slightly better than those of the LBE and GKS methods at high Rayleigh numbers with the same mesh resolution.

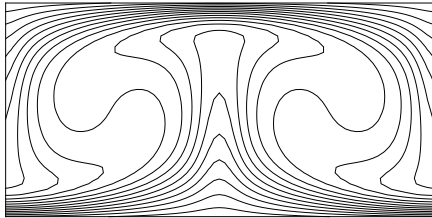
In order to understand the flow characters at different Rayleigh numbers, the isothermals and the streamlines at final steady states defined by Eq. (48)



(a) $Ra=5,000$



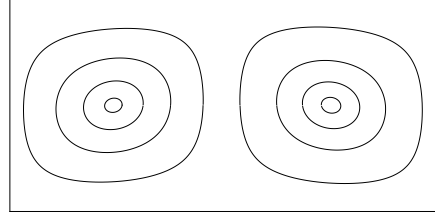
(b) $Ra=10,000$



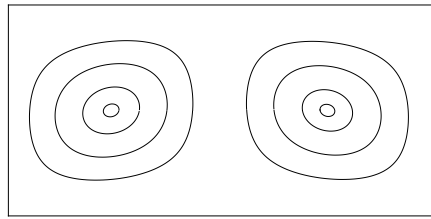
(c) $Ra=50,000$

Figure 7: Isothermals of the Rayleigh-Bénard convection at different Rayleigh numbers.

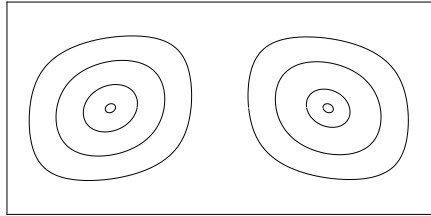
are presented in Figs. 7 and 8, respectively. It can be seen that as the Rayleigh number increases, two trends occur for the temperature distribution: enhanced mixing of the hot and cold fluids, and an increase in the temperature gradients near the bottom and top boundaries. Both trends enhance the heat transfer in the channel. These phenomena predicted by present model are well consistent with the results in the literatures [11, 12].



(a) Ra=5,000



(b) Ra=10,000



(c) Ra=50,000

Figure 8: Streamlines of the Rayleigh-Bénard convection at different Rayleigh numbers.

3.3. Natural convection in a square cavity

Natural convection in a square cavity is another canonical test case to validate the thermal model for Boussinesq flows. As illustrated in the Fig. 9, the configuration of the problem considered is a two-dimensional square cavity with a hot wall on the left side and a cool wall on the right. The Rayleigh number of the flow is defined by $Ra = g_0 \beta \Delta T H^3 / (\nu \kappa)$ where ΔT is the temperature difference between the hot and the cool wall, H is the height or width of the cavity.

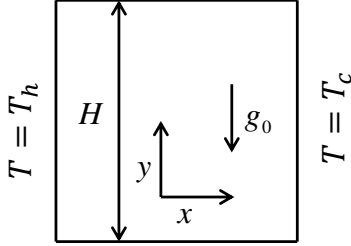


Figure 9: Schematic illustration of the flow domain for the natural convection in a square cavity.

We first consider the laminar natural convection where the Rayleigh number is less than 10^6 . In the simulations, an uniform mesh of 128×128 points is employed and RT_0 is set to be 10 to make the flow satisfy the incompressible limit. In addition, all the velocities obtained are normalized with the referenced velocity $U_0 = \kappa/H$. The velocity boundary condition, Eqs. (42), is applied to the four walls, the temperature boundary conditions, Eq. (43) and (44), are applied to the horizontal and vertical walls, respectively.

Figures. 10 and 11 show isothermals and streamlines for $Ra = 10^3, 10^4, 10^5$ and 10^6 under the steady state defined by Eq. (48). It can be seen that as Ra increases, isotherms change from almost vertical to be horizontal in the center of the cavity, and are vertical only in the thin boundary layers near the hot and cold walls. It means that the dominant heat transfer mechanism changes from conduction to convection. Correspondingly, a central vortex appears as the typical features of the flow. The vortex tends to become elliptic and breaks up into two vortices as Ra increases. All those phenomena agree well with those reported in the literatures [13, 17].

To quantify the results, we compare some quantities of interest with the benchmark results, including the maximum horizontal velocity on the vertical centerline of the cavity, u_{max} , and the corresponding y -coordinate, the maximum vertical velocity on the horizontal centerline of the cavity, v_{max} , and the corresponding x -coordinate, the maximum value of local Nusselt number on the

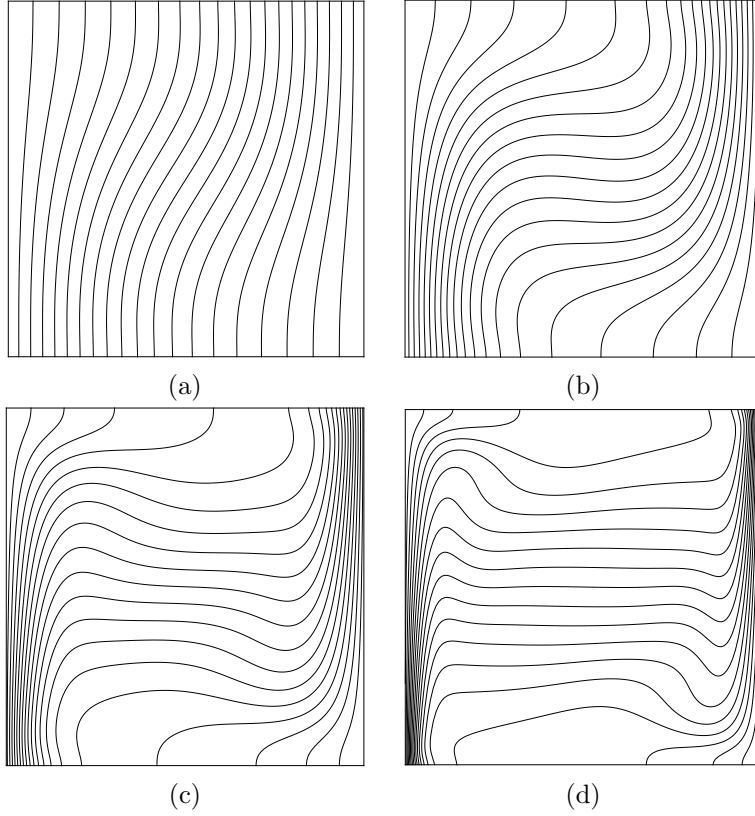


Figure 10: Isotherms of the natural convection for (a) $Ra = 10^3$, (b) $Ra = 10^4$, (c) $Ra = 10^5$ and (d) $Ra = 10^6$ with a uniform mesh of 128×128 points.

cool boundary, Nu_{max} , and the corresponding y -coordinate, and the averaged Nusselt number throughout the cavity \overline{Nu} . Table 2 compares the predictions from the present calculations with the literature results, also included are the relative errors. It is clearly observed that the present results are in excellent agreement with the reference solutions.

In order to further test the capability of the present DUGKS for simulating thermal flows, we now apply it to simulate the turbulent natural convection at high Rayleigh numbers. In such cases, thinning boundary layers along the hot and cool walls occur in which steeper velocity and temperature gradients appear, and fine mesh resolutions should be used. The FV nature of the DUGKS makes

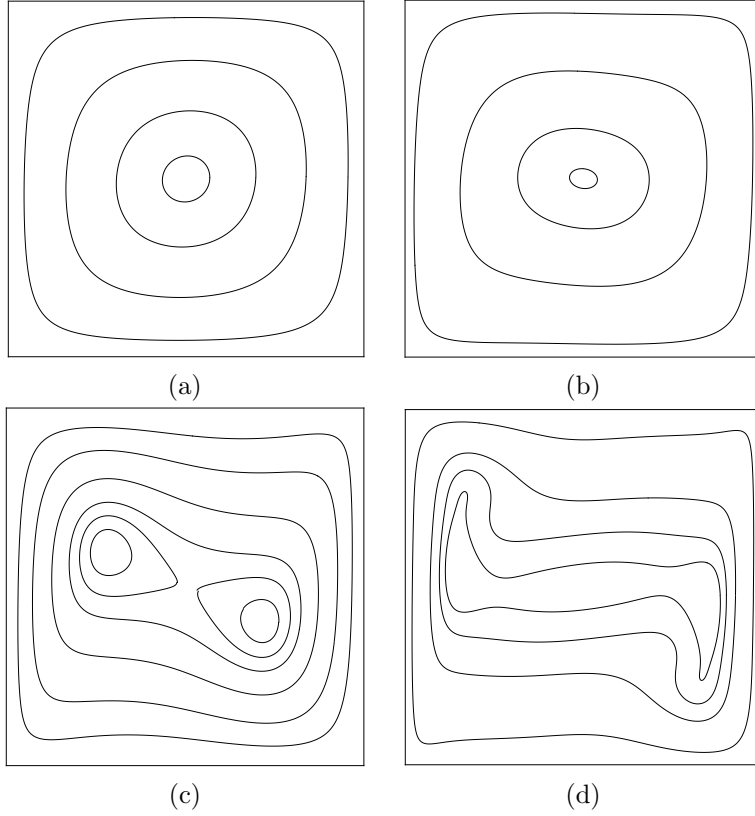


Figure 11: Streamlines of the natural convection for (a) $Ra = 10^3$, (b) $Ra = 10^4$, (c) $Ra = 10^5$ and (d) $Ra = 10^6$ with a uniform mesh of 128×128 points.

it easy to vary the mesh resolution according to the local accuracy requirement. In the current test, a non-uniform mesh is adopted, as shown in Fig. 12, where the mesh resolution follows a geometric progression for the grid spacing.

Figure. 13 shows instantaneous isothermals and streamlines at $Ra = 10^8$ and 10^{10} . As show, at $Ra = 10^8$, the isothermals are horizontal at the center of the cavity and become vertical near the hot and cool walls; the vortices appear at the top-left and lower-right corner due to the fast moving of the fluid near the walls. As Ra increase to 10^{10} , the isotherms at the center region of cavity are not straight longer and present a wavy state, while become irregular at the top-left and bottom-right corners of cavity; and the small-scale vortices occur in

Table 2: Comparison of the numerical results of the coupled DUGKS with those reported in the literature [28].

Ra		10^3	10^4	10^5	10^6
u_{max}	Present	3.6445	16.1737	34.8016	63.758
	[28]	3.649	16.178	34.73	64.63
Error(%)		0.123	0.025	0.223	1.35
y	Present	0.8203	0.8281	0.8594	0.8594
	[28]	0.813	0.823	0.855	0.850
Error(%)		0.898	0.620	0.515	1.11
v_{max}	Present	3.6989	19.6194	68.3318	215.5081
	[28]	3.697	19.617	68.59	219.36
Error(%)		0.0514	0.012	0.376	1.76
x	Present	0.1797	0.125	0.0703	0.0391
	[28]	0.178	0.119	0.066	0.0379
Error(%)		0.952	5.04	6.515	3.17
Nu_{max}	Present	1.5080	3.5313	7.6555	16.6194
	[28]	1.505	3.328	7.717	17.925
Error(%)		0.199	0.094	0.796	7.28
y	Present	0.9141	0.8594	0.9219	0.9531
	[28]	0.908	0.857	0.919	0.9622
Error(%)		6.72	0.280	0.316	0.946
\overline{Nu}	Present	1.1181	2.2431	4.5024	8.6796
	[28]	1.118	2.243	4.519	8.8
Error(%)		0.00894	0.004	0.367	1.37

entire simulation domain and the flow structure becomes irregular and chaotic.

All those observations agree well with the previous results [29, 30, 31].

Quantificationally, we measure some time-average qualities [30], such as the maximum horizontal velocity on the vertical centerline of the cavity, u_{max} , and the corresponding y -coordinate, the maximum vertical velocity on the horizontal centerline of the cavity, v_{max} , and the corresponding x -coordinate, and the average Nusselt number on the hot wall (\overline{Nu}). Table 3 gives the results calculated by the present method, also included are the results obtained from the pseudo-spectral method [32] and the LBE method with finer mesh resolutions [29]. As shown in the table, the obtained results are in good agreement with those reported in the literatures. It must be emphasized that no turbulence model is employed in the present simulation and the FV nature of DUGKS makes it easy to adopt non-uniform meshes.

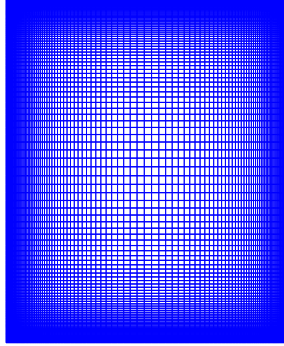


Figure 12: Numerical mesh with 128×128 grid points for the turbulent natural convection calculations

Table 3: Comparison of the numerical results of the present work with those reported in the literatures.

Ra		10^8	10^{10}
\bar{u}_{max}	Present	332.2619	2334.7
	[32]	321.876	—
	[29]	389.877	2323
y_{max}	Present	0.9396	0.9436
	[32]	0.928	—
	[29]	0.937	0.9423
\bar{v}_{max}	Present	2229.7	22282
	[32]	2222.39	—
	[29]	2231.374	21463
x_{max}	Present	0.0123	0.0039
	[32]	0.012	—
	[29]	0.0112	0.0049
\overline{Nu}	Present	30.5041	103.7467
	[32]	30.225	—
	[29]	30.506	103.663

Numerical instability has been a primary concern in previous thermal kinetic methods. Now, we compare the stability of present model with the well-accepted thermal LBE model (CLBGK) [13] under the same initial state and boundary conditions without considering the accuracy of the results. First, we measure the minimum required mesh resolution at a fixed Rayleigh number under steady

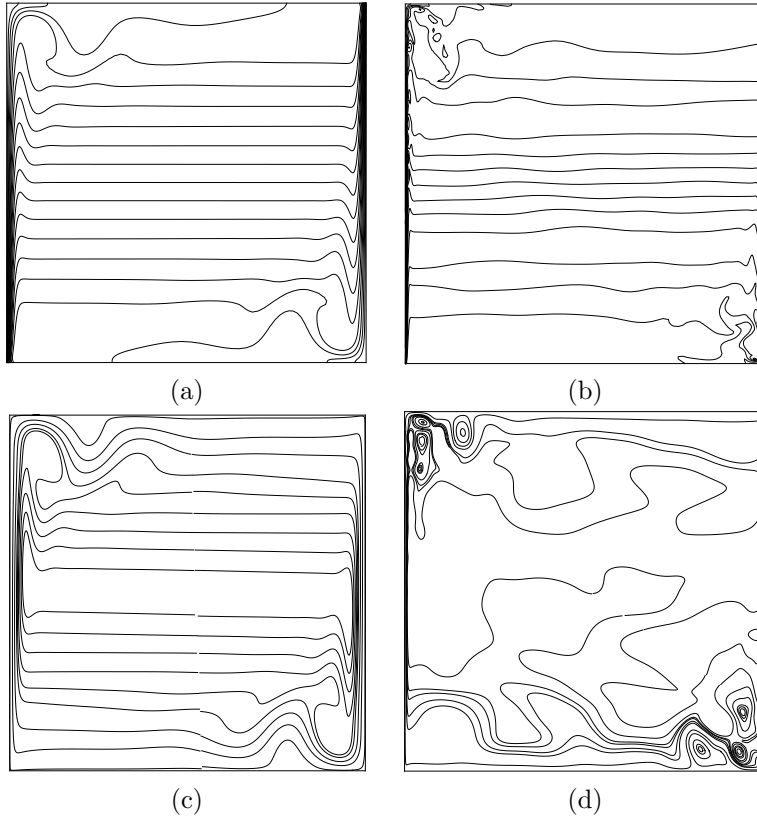


Figure 13: Isotherms for (a) $Ra = 10^8$, and (b) $Ra = 10^{10}$, and streamlines for (c) $Ra = 10^8$, and (d) $Ra = 10^{10}$ in the natural convection with a non-uniform mesh of 128×128 points.

state criterion of Eq. (48). Table 4 shows the minimum required mesh resolution at the given Rayleigh numbers. It can be seen that the DUGKS requires much less mesh points than the CLBGK in order to get a stable solution. For example, even at $Ra = 10^6$, the DUGKS can reach a steady state solution with 10×10 uniform mesh points. Second, we evaluate the maximum Rayleigh number on a specific mesh resolution at which the computation is still stable. It is found that with a fixed mesh resolution, the DUGKS can reach a much higher Ra than the CLBGK. For instance, on a uniform 32×32 mesh points, the computation from the CLBGK blows up at $Ra = 10^5$. However, the coupled DUGKS works even at $Ra = 10^{12}$. Clearly, in comparison with the CLBGK, the DUGKS has super

performance in stability. However, in terms of the computational efficiency, the CLBGK is about three times faster than the DUGKS for each node updating per time step due to the additional equilibrium distribution evaluation in DUGKS in order to include the collision effect into its flux transport. This is consistent with previous results for isothermal flows [22].

Table 4: The minimum required mesh resolution at different Rayleigh numbers.

Ra	CLBGK	DUGKS
10^4	20×20	5×5
10^5	30×30	10×10
10^6	60×60	10×10

4. Conclusions

In this paper, a coupled discrete unified gas-kinetic scheme is developed for the Boussinesq flows. The velocity field and temperature field are separately described by two distributions, and the DUGKS with an external force term is presented in the DUGKS algorithm. The simulation results demonstrate that the coupled DUGKS is of second order accuracy, and can accurately describe the laminar and turbulent thermal convection. Particularly, in comparison with the LBE methods, the coupled DUGKS can adopt the non-uniform mesh in a natural way, and has a remarkable performance in terms of the numerical stability .

ACKNOWLEDGMENT

This study is financially supported by the National Natural Science Foundation of China (Grant No. 51125024) and the Fundamental Research Funds for the Central Universities (Grant No. 2014TS119).

References

References

- [1] D. H. Rothman, S. Zaleski, Lattice-gas cellular automata: simple models of complex hydrodynamics, Vol. 5, Cambridge University Press, 2004.

- [2] S. Succi, *The Lattice-Boltzmann Equation*, Oxford university press, Oxford, 2001.
- [3] Z. Guo, C. Shu, *Lattice Boltzmann method and its applications in engineering (advances in computational fluid dynamics)*, World Scientific Publishing Company, 2013.
- [4] K. Xu, A gas-kinetic BGK scheme for the Navier–Stokes equations and its connection with artificial dissipation and Godunov method, *Journal of Computational Physics* 171 (1) (2001) 289–335.
- [5] K. Xu, J.-C. Huang, A unified gas-kinetic scheme for continuum and rarefied flows, *Journal of Computational Physics* 229 (20) (2010) 7747–7764.
- [6] Z. Guo, K. Xu, R. Wang, Discrete unified gas kinetic scheme for all knudsen number flows: Low-speed isothermal case, *Physical Review E* 88 (3) (2013) 033305.
- [7] Z. Guo, R. Wang, K. Xu, Discrete unified gas kinetic scheme for all Knudsen number flows: Ii. Compressible case, arXiv preprint arXiv:1406.5668.
- [8] R. A. Gingold, J. J. Monaghan, Smoothed particle hydrodynamics: theory and application to non-spherical stars, *Monthly notices of the royal astronomical society* 181 (3) (1977) 375–389.
- [9] K. Xu, X. He, Lattice Boltzmann method and gas-kinetic BGK scheme in the low-mach number viscous flow simulations, *Journal of Computational Physics* 190 (1) (2003) 100–117.
- [10] Z. Guo, H. Liu, L.-S. Luo, K. Xu, A comparative study of the LBE and GKS methods for 2D near incompressible laminar flows, *Journal of Computational Physics* 227 (10) (2008) 4955–4976.
- [11] X. Shan, Simulation of Rayleigh–Bénard convection using a lattice Boltzmann method, *Physical Review E* 55 (3) (1997) 2780.

- [12] K. Xu, S. H. Lui, Rayleigh-Bénard simulation using the gas-kinetic Bhatnagar-Gross-Krook scheme in the incompressible limit, *Physical Review E* 60 (1) (1999) 464.
- [13] Z. Guo, B. Shi, C. Zheng, A coupled lattice BGK model for the Boussinesq equations, *International Journal for Numerical Methods in Fluids* 39 (4) (2002) 325–342.
- [14] Y. Shi, T. Zhao, Z. Guo, Finite difference-based lattice Boltzmann simulation of natural convection heat transfer in a horizontal concentric annulus, *Computers & Fluids* 35 (1) (2006) 1–15.
- [15] Z. Guo, C. Zheng, B. Shi, T.-S. Zhao, Thermal lattice Boltzmann equation for low mach number flows: decoupling model, *physical review E* 75 (3) (2007) 036704.
- [16] X. He, S. Chen, G. D. Doolen, A novel thermal model for the lattice Boltzmann method in incompressible limit, *Journal of Computational Physics* 146 (1) (1998) 282–300.
- [17] J. Wang, D. Wang, P. Lallemand, L.-S. Luo, Lattice Boltzmann simulations of thermal convective flows in two dimensions, *Computers & Mathematics with Applications* 65 (2) (2013) 262–286.
- [18] P.-H. Kao, R.-J. Yang, Simulating oscillatory flows in Rayleigh-Benard convection using the lattice Boltzmann method, *International Journal of Heat and Mass Transfer* 50 (17) (2007) 3315–3328.
- [19] Y. Shi, T. Zhao, Z. Guo, Thermal lattice Bhatnagar-Gross-Krook model for flows with viscous heat dissipation in the incompressible limit, *Physical Review E* 70 (6) (2004) 066310.
- [20] T. Watanabe, Flow pattern and heat transfer rate in Rayleigh–Benard convection, *Physics of Fluids (1994-present)* 16 (4) (2004) 972–978.

- [21] C. Shu, X. Niu, Y. Chew, A lattice Boltzmann kinetic model for microflow and heat transfer, *Journal of statistical physics* 121 (1-2) (2005) 239–255.
- [22] P. Wang, L. Z. Z. Guo, K. Xu, A comparative study of LBE and DUGKS methods for nearly incompressible flows.
- [23] R. Mei, L.-S. Luo, W. Shyy, An accurate curved boundary treatment in the lattice Boltzmann method, *Journal of Computational Physics* 155 (2) (1999) 307–330.
- [24] Q. Zou, X. He, On pressure and velocity boundary conditions for the lattice Boltzmann BGK model, *Physics of Fluids (1994-present)* 9 (6) (1997) 1591–1598.
- [25] T. Zhang, B. Shi, Z. Guo, Z. Chai, J. Lu, General bounce-back scheme for concentration boundary condition in the lattice-Boltzmann method, *Physical Review E* 85 (1) (2012) 016701.
- [26] W. Reid, D. Harris, Some further results on the Bénard problem, *Physics of Fluids (1958-1988)* 1 (2) (1958) 102–110.
- [27] R. Clever, F. Busse, Transition to time-dependent convection, *J. Fluid Mech* 65 (4) (1974) 625–645.
- [28] G. de Vahl Davis, Natural convection of air in a square cavity: a benchmark numerical solution, *International Journal for Numerical Methods in Fluids* 3 (3) (1983) 249–264.
- [29] H. Dixit, V. Babu, Simulation of high Rayleigh number natural convection in a square cavity using the lattice Boltzmann method, *International journal of heat and mass transfer* 49 (3) (2006) 727–739.
- [30] C. Zhuo, C. Zhong, Les-based filter-matrix lattice Boltzmann model for simulating turbulent natural convection in a square cavity, *International Journal of Heat and Fluid Flow* 42 (2013) 10–22.

- [31] D. Contrino, P. Lallemand, P. Asinari, L.-S. Luo, Lattice-Boltzmann simulations of the thermally driven 2D square cavity at high Rayleigh numbers, *Journal of Computational Physics* 275 (2014) 257–272.
- [32] P. Le Quéré, Accurate solutions to the square thermally driven cavity at high Rayleigh number, *Computers & Fluids* 20 (1) (1991) 29–41.